Estimation of top tensions in mooring lines by sensor fusion

Thomas Sauder [a,b,*], Philippe Mainçon [a,c], Erling Lone [b], Bernt J. Leira [b]

[a] *SINTEF Ocean, P.O. Box 4762 Torgarden, 7465 Trondheim, Norway*
[b] *NTNU, Trondheim, Norway*
[c] *SINTEF Industry, P.O. Box 4760 Torgarden, 7465 Trondheim, Norway*

ARTICLE INFO

ABSTRACT

The paper describes a sensor fusion method that provides reliable, uninterrupted and bias-free estimates of the top tension in a mooring line. The method exploits the geometric nonlinearity of mooring systems installed in shallow to moderate water depths: a change of line length (due to winching) affects the local dynamic stiffness of the mooring line. Based on measurements of fairlead displacements and of the dynamic part of the top tension, the line length and true (unbiased) mean tension can be inferred. The method combines the use of (1) a classical kinematic observer to derive fairlead motions, (2) the compression of the recent history of fairlead motions to a few parameters, (3) a bank of neural networks, each network modelling the response corresponding to a given line length/static tension, and (4) a heuristic approach to selecting the most promising model among the candidates. One major advantage of the method is its sparsity, making it computationally efficient so it can be applied both offline, on large sets of recorded historical data, and online running on lightweight embedded hardware. The paper presents in detail each component listed above, and the method as a whole is verified on a realistic case. Given that enough excitation is present, the estimator was found to converge towards the true value of the tension, and to cope well with transient conditions such as winching operations, and with the presence of oceanic current.

1. Introduction

1.1. Background

Lifetime extension of ageing floating oil and gas production units (FPU) installed on the Norwegian Continental Shelf has led to a reassessment of existing mooring systems. Mooring chains have been particularly scrutinized as they have been failing at a much higher rate than targeted by regulatory bodies [1,2]. In the wake of several joint industry projects and research projects on this topic, such as Normoor [3], FoCCs [4], TWI [5], Exwave [6], among others, the LIFEMOOR project, which supports the present research, aims at understanding the interaction of load history, wear, corrosion, and crack initiation/propagation in mooring chains. It is now established that the fatigue capacity of mooring chains deteriorates when operating at increasing *mean* tensions [7], a phenomenon not accounted for in S-N curves used in mooring design. A key result of LIFEMOOR has been that, for FPU such as semi-submersibles, this mean tension dependency has a significant impact on the actual fatigue damage on mooring, and hence remaining fatigue capacity and possible life extension [8]. The key reason for that is that such FPUs generally operate at mean tensions well below those used to establish design S-N curves.

* Corresponding author at: SINTEF Ocean, P.O. Box 4762 Torgarden, 7465 Trondheim, Norway.
  E-mail addresses: thomas.sauder@sintef.no (T. Sauder), philippe.maincon@sintef.no (P. Mainçon), erling.lone@ntnu.no (E. Lone), bernt.leira@ntnu.no (B.J. Leira).
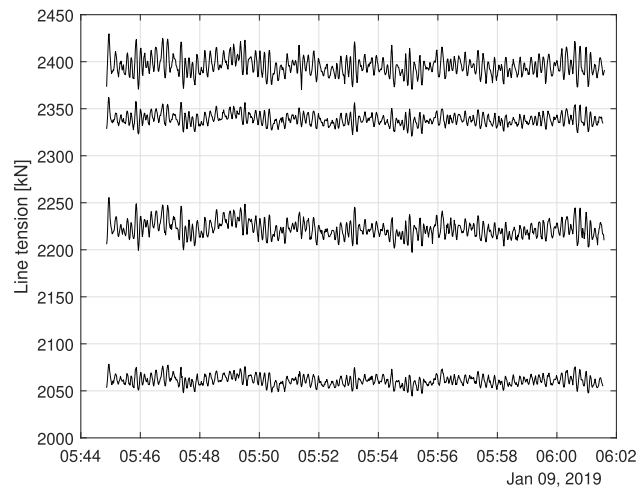
Fig. 1. Tension group 4.

Based on this finding, the present research aimed at obtaining reliable estimates of the *actual load history* (mean and dynamic tension) experienced by a mooring line, to support lifetime extension assessments. Norwegian authorities require all FPU operating on the Norwegian Continental Shelf to be equipped with sensors that monitor the tension in mooring lines at the fairlead or winch level, referred to as top tension [9, §12]. These sensors must be calibrated on a yearly basis [9, §15], meaning that the multiplicative factor between the electrical signal delivered by the sensor [mV] and the tension [kN], must be controlled, and adjusted if necessary. However, general experience and field reports [1,10,11] concur to the fact that the sensors, albeit well calibrated, often generate signals that are noisy and biased, i.e. polluted by slowly-varying additive error.

The estimation and removal of such biases is particularly challenging, since winching the mooring line in or out has the same static effect on the top tension measurement as sensor bias. Furthermore, since the amount of winching is not systematically documented over the years, the exact mean tension in the line becomes uncertain [1]. As an illustration, Fig. 1 shows low-pass filtered top-tension measurement for four mooring lines that are part of the same bundle, at the corner of a semi-submersible. Large differences (350 kN) in measured mean tension may be due to different line length (winching) or to sensor bias. This uncertainty will in turn affect the fatigue damage assessments: for the tension measurements shown in Fig. 1, the observed difference in mean load level is about 2% of the minimum breaking load, and yields about 20% difference in the predicted fatigue capacity [7], and about one order of magnitude difference in the estimated fatigue failure probability [12].

A natural question is then whether top tension can be estimated in other ways than by direct measurement. For mooring lines based on chains and steel rope, the dynamic tension along the line can be satisfactorily estimated numerically, by using nonlinear finite element analyses. This assumes that the model of the full-scale system is correctly modelled. Examples of successful comparisons with full-scale and model scale measurements are given in [13,14], respectively, where motions of the fairlead have been prescribed, and top tensions compared. In these examples, the exact wave and current kinematics are of secondary importance,[1] and the main modelling parameters are the segments' length, mass distribution, added-mass and drag coefficients. Once these are selected, the model requires accurate fairlead motion time series. Mooring lines exhibit (1) nonlinear restoring characteristics and (2) a significant rate dependency due to inertia, hydrodynamic drag and added-mass loads. Therefore both (1) the slowly-varying (large-amplitude) motions that cause a varying local stiffness, and (2) the wave-frequency (lower-amplitude) motions of the fairlead should be captured. The latter should be sampled at a frequency well above the wave frequency, so that velocity and accelerations can be correctly estimated. Such information as a whole is usually not directly available from measurements.

Table 1 shows the available sources of information about the tension in mooring lines on a typical FPU. While none of them can independently provide reliable, bias-free, estimate of top tension, and hence fatigue damage in mooring lines, they provide complementary information.

The present paper describes a sensor fusion[2] method that provides reliable, uninterrupted and bias-free estimate of the top tension in a mooring line. One major advantage of the method is its sparsity, making it computationally efficient so it can be applied offline, on large sets of recorded historical data, and online, running on a lightweight embedded system. The main idea is to exploit the geometric nonlinearity of mooring systems installed in shallow to moderate water depths: a change of line length (due to winching) affects the local dynamic stiffness of the mooring line, and hence the dynamic tension. Based on independent measurements of fairlead displacements and dynamic top tension, the line length and true (unbiased) mean tension can be inferred. As the present

---

[1] Note that this might not be true for other types of slender marine structures, such as large diameter risers for which ambient water particle kinematics is of importance.

[2] Or more correctly information fusion, as first-principle-based numerical models are involved.

Table 1
Direct and indirect sources of information about top tension in a mooring line.

Information source	Obtained value	Strengths and weaknesses
Tension measurements at fairlead	Tension at fairlead	(+) Calibration factor checked on a regular basis (−) Bias in measurement and winching have the same static effect, making mean tension difficult to track (−) Presence of noise
Nonlinear FEM using prescribed motions at fairlead	(1) Tension at fairlead (2) Any other structural response in the line	(+) Proven/validated method to describe dynamic tension in mooring lines (−) Not suitable to work with noisy fairlead displacement measurements (−) Not designed to run in real-time as it relies on Newton–Raphson iterations (−) Requires mooring line properties (incl. length) to be known
Global positioning system (GPS)/real-time kinematic positioning (RTK)	Position of vessel	(+) No drift/bias (−) Accuracy and update frequency (1–2 Hz) not adequate to estimate velocity/acceleration by differentiation (−) Subject to intermittent signal loss due to e.g variable atmospheric conditions
Inertial Measurement Unit (incl. accelerometer, gyrometer, magnetometer/fluxgate compass)	(1) Attitude (e.g. Euler angles) (2) Angular velocities (roll, pitch, yaw rates) (3) Linear accelerations (surge, sway, heave)	(+) High-frequency signals (−) Presence of acceleration due to gravity in acc. signal (−) Bias due to mounting misalignment, changing declination, and other phenomena (−) Presence of noise

work encompasses many fields (structural dynamics, state estimation, signal compression, artificial neural networks), we will discuss relevant previous work in the main text, when corresponding concepts are introduced.

Section 2 describes the proposed method. Section 3 presents case study that illustrates its capabilities and performance on a realistic case. Conclusions and perspectives are outlined in Section 4.

2. Method description

2.1. Overall description

The dynamic behaviour of mooring lines in shallow to moderate water depths depends on the line configuration. This is often referred to as a geometric non-linearity, and means that given a prescribed top-end motion, the *dynamic* tension at the fairlead depends on the line length. We recall that the objective of the present work is to infer the actual line length (and hence the unbiased mean tension) by studying the relationship between top motions and measured dynamic tension.

To this effect, high-frequency uninterrupted fairlead motions are obtained by fusing global and inertial navigation systems that are commonly embedded on FPUs. Then, for each line, these motions are used to compute the top tension of N_c line *candidates*. The candidates differ by the length of the top segment, i.e. the uncertain quantity to be estimated. The dynamic tension obtained with each of the N_c model candidates is then compared to the measured dynamic tension. The models that provide the best match are used to infer the true tension in the line.

The main components of the method are shown in the block diagram in Fig. 2. They will be briefly described now, while details will be given in the next subsections. (1) A classical kinematic observer, fed by GPS and inertial measurement unit (IMU) measurements, is used to estimate fairlead motions. These are then expressed in a suitably-chosen coordinate system for the line. Then (2) a signal compression method, named here "tadpole compression", summarizes the *recent* history of fairlead motions by a sparse set of parameters p. These parameters feed (3) a bank of N_c artificial neural networks (ANN), trained using nonlinear finite element model candidates, predicting top tensions $\hat{F}_i$ for $i \in \{1, \dots, N_c\}$ from the tadpole parameter. Note that thanks to the sparsity of (2), the ANN are extremely sparse too. Finally, (4) a tension estimator combines tension measurements with the predictions, and outputs an unbiased tension estimate $\hat{F}$. This estimate can be used in fatigue assessment. Note that both measurements and predictions are (5) band-pass-filtered to keep only the dynamic tension in the comparison. These components will be described in detail in the following.

2.2. Coordinate systems

Three reference frames and associated right-handed coordinate systems will be used in the following. The notations are borrowed from [15, Chapter 2]. The Earth-fixed inertial frame of reference $\{n\}$, represented in blue in Fig. 3, has the coordinate system (n_1, n_2, n_3) where n_1 points towards the North, n_2 towards the East, and n_3 downwards. A body-fixed non-inertial frame of reference, $\{b\}$, centered at the FPU center (arbitrarily chosen) and represented in black in Fig. 3, has the coordinate system (b_1, b_2, b_3) where these units vectors define surge, sway and heave respectively. Finally, $\{f^{(i)}\}$, represented in red for one line i in Fig. 3, is an Earth-fixed frame of reference, with a coordinate system which origin $F_0^{(i)}$ lies at the fairlead i when the platform is at rest. Its position expressed in $\{n\}$ is $p_0^{(i)} \in \mathbb{R}^3$. A coordinate system $(f_1^{(i)}, f_2^{(i)}, f_3^{(i)})$ is associated to $\{\mathbf{f^{(i)}}\}$ where $f_1^{(i)}$ is horizontal and in the plane defined by the mooring line at rest, and points away from the anchor. $f_3^{(i)}$ is located in the same plane and points downwards. $f_2^{(i)}$ is obtained by requiring that the coordinate system is right-handed. When the platform is moving, $\overrightarrow{F_0^{(i)}F^{(i)}}$ along $f_1^{(i)} f_2^{(i)}$ and $f_3^{(i)}$ respectively describe in-line horizontal, transverse, and in-line vertical motions of the fairlead. A displacement of the fairlead along positive f_1 or negative f_3 stretches the mooring line in its plane.
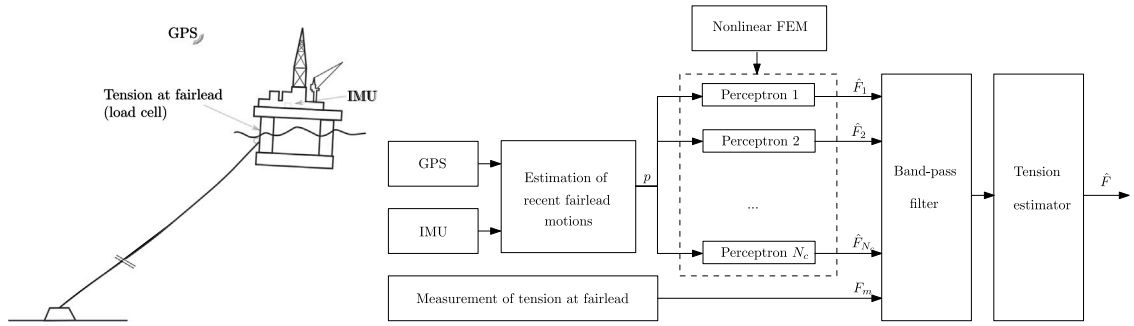
Fig. 2. Overall system architecture, represented as a block diagram (right-hand side). The left-hand side of the figure shows the location of the sensors on the floating platform.
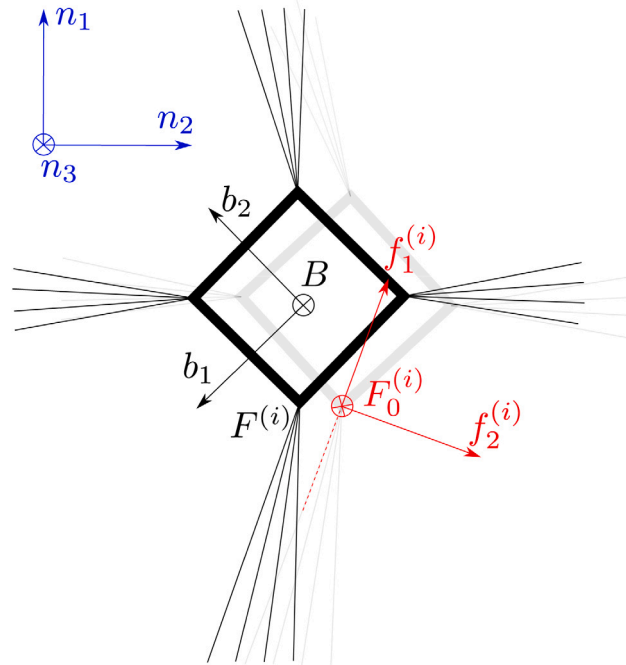

Fig. 3. Coordinate systems $\{n\}$, $\{b\}$, and $\{f^{(i)}\}$. The grey contour represents the platform and mooring at rest. Note that for clarity, the platform is not represented with any roll or pitch angle, here. In general b_3 is not necessarily vertical. $F^{(i)}$ denotes the fairlead of the ith mooring line.

2.3. Robust estimation of fairlead motions

The objective is to obtain a robust high-frequency estimation of fairlead motions, by fusing global positioning system (such as GPS) and strap-down inertial systems (IMU). Main kinematic quantities are defined in Table 2. $R_b^n(\Theta)$ is the rotation matrix from $\{b\}$ to $\{n\}$, where Θ expresses the attitude of the platform in terms of Euler angles (Tait–Bryan angles), see Eq. (1). The matrix $T_b^n(\Theta)$, whose expression is given in Eq. (2), relates the body-fixed angular velocity vector to the rate of change of Euler angles by $\dot{\Theta} = T_b^n(\Theta)\omega$.

$$R_b^n = \begin{pmatrix} \cos\psi\cos\theta & -\sin\psi\cos\phi + \cos\psi\sin\theta\sin\phi & \sin\psi\sin\phi + \cos\psi\cos\phi\sin\theta \\ \sin\psi\cos\theta & \cos\psi\cos\phi + \sin\phi\sin\theta\sin\psi & -\cos\psi\sin\phi + \sin\psi\cos\phi\sin\theta \\ -\sin\theta & \cos\theta\sin\phi & \cos\theta\cos\phi \end{pmatrix} \tag{1}$$

$$T_b^n = \begin{pmatrix} 1 & \sin\phi\tan\theta & \cos\phi\tan\theta \\ 0 & \cos\phi & -\sin\phi \\ 0 & \frac{\sin\phi}{\cos\theta} & \frac{\cos\phi}{\cos\theta} \end{pmatrix} \tag{2}$$

The position p^n is typically obtained at a low frequency (typically 0.5–2 Hz) and with short-term signal losses, from a global positioning system, and the attitude Θ is provided by motion reference unit (MRU) which includes a compass/magnetometer at the

Table 2

Notations.

Symbol	Description
$p^n = (N, E, D)^\top \in \mathbb{R}^3$	North-East-Down position vector of the platform center B, expressed in $\{n\}$
$\Theta = (\phi, \theta, \psi)^\top \in SO(3)$	Attitude (Euler angle)
$V = (u, v, w)^\top \in \mathbb{R}^3$	Body-fixed linear velocity of platform center expressed in $\{b\}$ (surge, sway, heave)
$\omega = (p, q, r)^\top \in \mathbb{R}^3$	Body-fixed angular velocity (roll, pitch, yaw)
$r_a \in \mathbb{R}^3$	Position of accelerometer expressed in $\{b\}$
$a = (a_1, a_2, a_3)^\top \in \mathbb{R}^3$	Body-fixed linear acceleration at accelerometer expressed in $\{b\}$
$b_{acc} \in \mathbb{R}^3$	Accelerometer measurement bias expressed in $\{b\}$
$b_{gyro} \in \mathbb{R}^3$	Gyrometer measurement bias expressed in $\{b\}$
$g = (0, 0, 9.81 \text{ m/s}^2)$	Acceleration of gravity expressed in $\{n\}$

Table 3

List of mooring lines considered in the present study.

Line	Azimuth [°]	Horiz. dist. fairlead-anchor [m]	Fairlead b1 [m]	Fairlead b2 [m]	Line length [m]	Pretension [kN]	Cluster
1	182.5	1255.4	46.8	−49.1	1347.5	2156	South
5	262.5	1249.9	52.7	42.5	1347.5	1957	West
9	342.5	1248.4	−46.4	49.4	1340.8	2150	North
13	82.5	865.9	−52.7	−42.5	950.8	2184	East

same time instants. The origin and coordinate system of $\{b\}$ follows the position and orientation of the sensor. The three-components gyro, which can be located in any position of the (rigid) floater, provides a biased[3] measurement of ω. Finally, an accelerometer, located at a known position $r_{acc} \in \mathbb{R}^3$ expressed in $\{b\}$, provides a three-component measurement of the acceleration that is affected by the presence of the acceleration of gravity, including a bias due to misalignment. Both accelerometer and gyro provide data at frequencies well above 10 Hz, typically 100–200 Hz. The objective is to fuse these measurements to obtain a high-frequency estimation of the position and attitude of the floater.

In the following $\hat{\cdot}$ denotes *estimated* quantities. Given the measured acceleration a_m, the estimated acceleration is $\hat{a} = a_m + (R_b^n)^\top g^n - b_{acc}$, where $g^n = (0, 0, 9.80685)^\top m.s^{-2}$. The various biases are estimated in real-time by solving $\dot{b} + b/T = k\varepsilon$, where ε is the driving error, and k and T are suitably chosen gains. The gyro bias b_{gyro} is estimated with $\varepsilon = (T_b^n)^{-1} \int T_b^n(\Theta)\omega - \Theta$. The velocity and accelerometer bias are estimated from the difference between integrated accelerations, and GPS positions. The estimated position $\hat{p}$ and attitude $\hat{\Theta}$ is obtained at high frequency by integrating the unbiased velocity. Then, the ith fairlead displacement $d^{(i)} \in \mathbb{R}^3$, expressed in $\{f\}$ is found by:

$$d^{(i)} = \left(R_{f^{(i)}}^n \right)^\top \left(\hat{p}^n + R_b^n(\hat{\Theta})(\overline{BF^{(i)}})^b - p_0^{(i)} \right) \tag{3}$$

where $R_{f^{(i)}}^n$ is the rotation matrix built by setting $\phi = 0$, $\theta = 0$, and $\psi = \psi^{(i)} - \pi$ in Eq. (1), where $\psi^{(i)}$ denotes the azimuth of line i, from fairlead to anchor, when the line is at rest (see for example Table 3). In the following, we will assume perfect $d^{(i)}$. The interested reader is referred to [15, Chap. 14] for a details about convergence and estimation errors.

2.4. Tadpole compression of recent fairlead motion history

Once displacements of the fairlead are obtained, the objective is to "summarize" these time series $d^{(i)}(t)$ by a few parameters, emphasizing the recent information. This summary $p(t)$ will be used to estimate the mooring line tension.

This follows an approach previously applied to other problems in [17]. Let $\mathcal{H}$ be the space of square-integrable functions on $(-\infty, 0]$. Given a bounded positive weight function $w(t)$ defined for $t \leq 0$, and two continuous signals f and g in $\mathcal{H}$, we define the inner product and associated distance

$$\langle f, g \rangle_w = \int_{-\infty}^{0} f(t)g(t)w(t)dt \tag{4}$$

$$\|f - g\|_w = \sqrt{\int_{-\infty}^{0} |f(t) - g(t)|^2 w(t)dt} \tag{5}$$

For a weight function of the form $w(t) = e^{t/t_m}$ with $t_m > 0$, the distance Eq. (5) measures how similar f and g are in the recent past. What is meant by *recent* is quantified by the mean lifetime parameter t_m: for example, differences between f and g at time instant $t = -\ln 2 \cdot t_m$, will be half as important as such differences occurring at $t = 0$.

The objective is to obtain a good approximation, with an emphasis on its recent past, of a function f of the (infinite-dimensional) vector space $\mathcal{H}$. This approximation is chosen as a linear combination $\sum_{i=1}^{n_p} p_i T_i(t)$, where the (finite) family of coefficients $(p_i)_{i \in \{1, \ldots, n_p\}}$

---

[3] See for example [16] for a discussion about the sources of gyro bias and their quantification.

provides a "summary" of the signal. One thus seeks a family of functions $(T_i)_{i \in \{1,\dots,n_p\}}$ spanning a finite-dimension subspace $\bar{\mathcal{H}}$ of $\mathcal{H}$, and a family of n_p parameters p_i that minimize

$$J = \|f - \sum_{i=1}^{n_p} p_i T_i(t)\|^2 = \|f\|_w^2 - 2 \sum_i \langle f, T_i \rangle_w + p_i^2 \sum_{i,j} \langle T_i, T_j \rangle_w \tag{6}$$

Assuming now that we have such a family (T_i) that is orthonormal with respect to the inner product defined in Eq. (4), that forms a basis of $\bar{\mathcal{H}}$, then $\forall i, j \in \{1, \dots, n_p\}, \langle T_i, T_j \rangle_w = \delta_{ij}$ (Kronecker delta). In this case, the coefficients p_i are obtained by projection $p_i = \langle f, T_i \rangle_w$. The distance (using the $\| \cdot \|_w$ norm) between two functions in $\mathcal{H}$ is equal to the euclidean distance between their respective "summaries" in $\mathbb{R}^{n_p}$.[4] Such an orthonormal family (T_i) can be obtained by choosing a set of linearly independent functions $(\tilde{T}_i)$ spanning a relevant subspace of $\mathcal{H}$, and performing a Gram–Schmidt w-orthonormalization using Eq. (4). While the latter step is straightforward, the choice of the subset spanning $\bar{\mathcal{H}}$ is of crucial importance as our approximation of f will necessarily be contained in this subset.

To make this choice, let the signal f be the history of one of the three components of the fairlead displacement. Mooring lines are subjected to high damping loads, so it is expected that the "memory" of the system (its nonlinear impulse response) is limited to a few seconds. Typical fairlead motions are also covering periods larger than the second. In the present work, the space spanned by exponential decay functions is chosen

$$\forall i \in \{1, \dots, n_p\}, \tilde{T}_i(t) = e^{\frac{i-1}{n_p-1}\frac{t}{t_c}} \tag{7}$$

with characteristic time $t_c = 1$ s, which are represented in Fig. 4 for $n_p = 6$. The figure also shows the weight function $w(t)$ with $t_m = 1.3$ s, the orthonormal basis (T_i), obtained by the Gram–Schmidt method, and the dual basis $(T_i^*)_{i \in \{1,\dots,n_p\}}$ of (T_i).

Using T_i^* and T_i as defined above, the compressed representation p of a signal f is obtained by:

$$p_i = \int_{-\infty}^{0} f(t) T_i^*(t) dt \tag{8}$$

The approximate signal $\hat{f}$ from p is synthesized as

$$\hat{f} = \sum_{i=1}^{n_p} p_i T_i(t) \tag{9}$$

Fig. 5 shows ten arbitrarily selected fairlead motion signals that have been compressed using Eq. (8) and synthesized using Eq. (9). Each component of the displacement, was originally described by 93 samples values (covering 9.2 s at 10 Hz), and is now summarized by only 6 parameters. The quality of the approximation is excellent in the near past, and degrades with the past time. The interested reader is referred to [17] for details regarding the discrete implementation of the method, including incremental update of the p_i coefficients using the latest displacement value only.

2.5. Functional relationship between p and F - a necessary condition

For at each time instant, for each mooring line, the tadpole coefficients $p(t) \in \mathbb{R}^{3n_p}$ provide a summary of the recent fairlead motions. The objective is to predict, at each time t, the top tension $F(t)$ from $p(t)$. If the behaviour of the mooring line is quasi-static, the instantaneous displacement $d^{(i)}(t)$ is sufficient to predict the tension. In that case, any tadpole compression would have the ability to predict the top tension. In general, however, the compressed data $p(t)$ must retain enough information about the recent past to predict the mooring line top tension. In other words, the decay times t_m and t_c, and the basis size n_p in Eq. (7) must be adequately chosen. If memory effects were significant, and if decay times were chosen too small, then a given recent motion summary $p(t)$ would result in different top tensions $F(t)$, depending on the motion history in the more remote past.

Therefore, to efficiently investigate whether a functional relationship between $p(t)$ and $F(t)$ *might* be established, an analysis based on comparative fractal dimensions is performed [17, Section 6.3]. The fundamental idea is that if $F(t)$ can unambiguously be predicted from $p(t)$, then the dimension of the manifold $\{p(t)\}_{t \geq 0}$ must remain nearly unchanged when augmenting it with the corresponding $F(t)$ values. What we refer to as the dimension here is the Minkowski–Bouligand dimension (a fractal dimension), estimated here from the distances between points in the manifolds. To illustrate this, consider two manifolds $\{x(t)\}_{t \geq 0}$ and $\{y(t)\}_{t \geq 0}$ in $\mathbb{R}^3$. If $\{x(t)\}_{t \geq 0}$ has a dimension 2 (i.e. forms a surface), a functional relationship between x and y might be achievable if $\{x(t), y(t)\}_{t \geq 0}$ remains a surface, and does not form a "cloud" of points (of dimension larger than 2). Note that this condition on the fractal dimension is necessary, but not sufficient: x and y could be manifolds of dimension 2, each containing random points in a defined plane.

Hence a necessary condition (on the decay times and basis size) to establish a functional relationship between $p(t)$ and $F(t)$ is that the fractal dimensions of the manifolds $\{p(t)\}_{t \geq 0}$ and $\{p(t), F(t)\}_{t \geq 0}$ are close to each other. A practical illustration of this check with actual data will be presented in Section 3.

---

[4] This property is important to prove convergence and hence the quality of the approximation, see [17] for details.
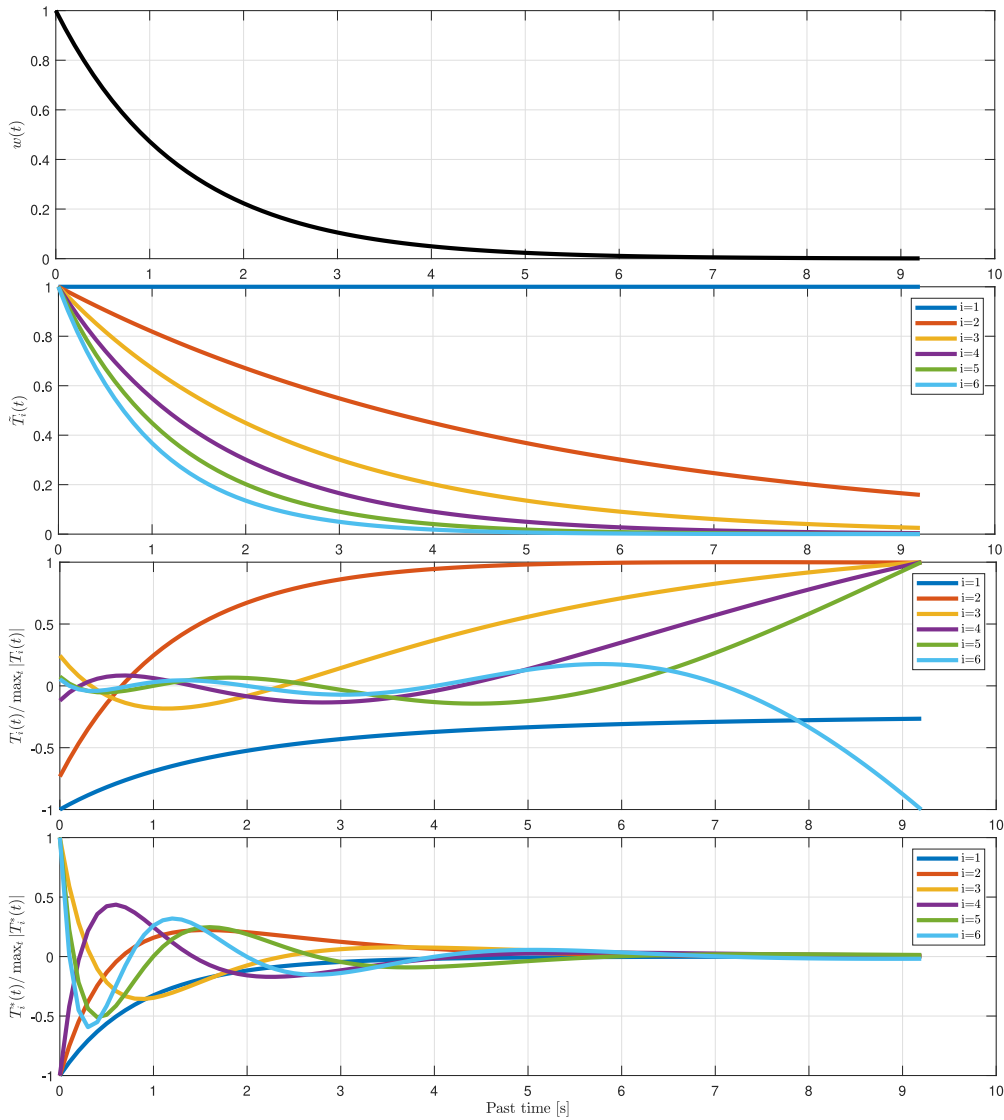
Fig. 4. From top to bottom: (1) weight function, (2) initial functions spanning $\tilde{\mathcal{H}}$, (3) orthonormal basis of $\tilde{\mathcal{H}}$, (4) dual basis (T_i^*) of (T_i).
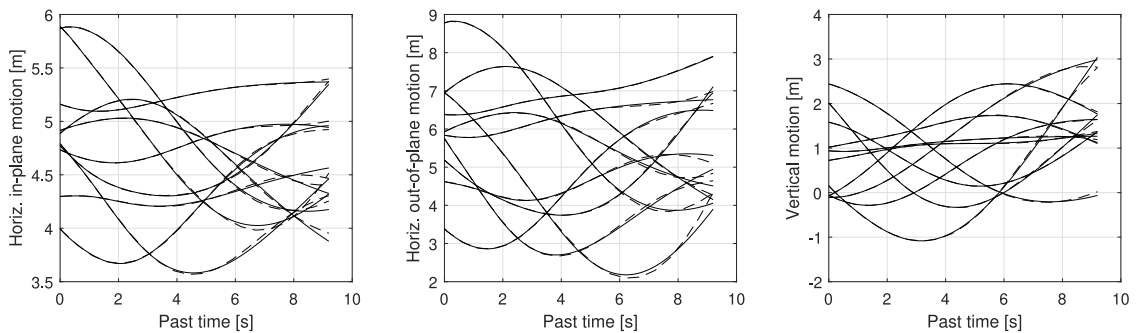

Fig. 5. Time series of fairlead displacements $d^{(i)} \in \mathbb{R}^3$, decomposed along $f_1^{(i)}$ (left plot), $f_2^{(i)}$ (middle plot) and $f_3^{(i)}$ (right plot). Each plots presents a comparison between compressed/synthesized signal $\hat{f}$ (solid line) and true signal f (dashed line). The name "tadpole compression" comes from the visual representation of these functions.
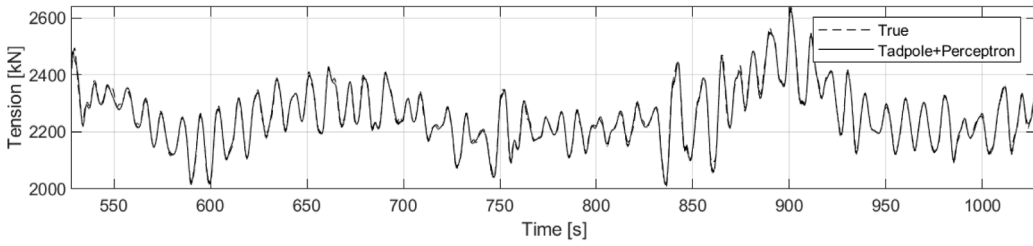
Fig. 6. Comparison between tensions calculated by RIFLEX (dashed line) and by the ANN fed with tadpole coefficients (full line), for a case not used in training.

2.6. Efficient prediction of top tension based on recent history of fairlead motion

Once it is established that $F(t) \in \mathbb{R}$ can be expressed as a function of $p(t) \in \mathbb{R}^{3n_p}$, the next objective is to attempt to construct such a function. The universal approximation theorem [18] states that a feed-forward artificial neural network (ANN) with a single hidden layer can approximate any continuous function. Hence $\hat{F} : \mathbb{R}^{3n_p} \to \mathbb{R}$ is formulated as such a network with n_h neurons in the hidden layer, and a hyperbolic tangent activation function σ. In other words, $\hat{F} = W_2 \circ \sigma \circ W_1$ where W_1 and W_2 are affine maps and $\circ$ denotes component-wise composition. Assuming a fully connected network, W_1 and W_2 are described by full matrices of dimensions $n_h \times (3n_p + 1)$ and $1 \times (n_h + 1)$, respectively, that is a total number of parameters equal to $n_h(3n_p + 2) + 1$, which amounts to 201 if $n_h = 10$.

The identification of these parameters, such that $\hat{F}$ satisfactorily links p to F is denoted the *training* phase. Based on N_{training} pairs $\{(p, F)_i\}_{i \leq N_{\text{training}}}$ obtained from nonlinear Finite Element simulations (here, RIFLEX [19]), $\sum_{i=1}^{N_{\text{training}}} [\hat{F}_i(p) - F_i(p)]^2$ is minimized using the Levenberg–Marquardt method. Once the training is carried out, the behaviour of the ANN is tested on a *validation* set, that is a set of $\{(p, F)_i\}_{i \leq N_{\text{validation}}}$ different from the training set. Fig. 6 shows an example of time series from the validation set, predicted independently by the ANN and by RIFLEX.

The idea of using ANN to predict mooring tension is not new [20–22], but in previous works, the input of the ANN consisted in time samples of the floater motions (with previous predicted tension values added in some cases). Due to the absence of compression, the dimension of the inputs to the ANN was significantly larger (28 for [21], 60 for [22], 300 for [20]). For the case with the less inputs, 100 neurons were used in the hidden layers [21], which leads to an ANN with about 40 times more parameters to calibrate than in the present work. When considering a single neural network such a difference is, in practice, insignificant in terms of computational time: ANNs runs several orders of magnitude faster than nonlinear FEM. However, sparsity is an advantage here as we will train and use *a bank* of ANNs.

Again, the overall objective is to infer the mooring line length (and therefore the unbiased top tension) based on measurements of motions and of the (biased) top tension. To this end, N_c separate neural networks are trained with similar p data, but with F data corresponding to different top segment lengths, typically $N_c = 10 - 15$ variations around the nominal value.[5] We will now show how using this bank of N_c neural networks allows to estimate the line length and the tension in near real time.

2.7. Top tension estimator based on measurements and bank of ANNs

At each time, the compressed recent history of motions, p estimated from Eq. (3) and (8), and the top tension are predicted in parallel for all N_c model line candidates $\hat{F}_j(p(t)), 1 \leq j \leq N_c$. The top tension $F_m(t)$ is measured at the fairlead. Both $\hat{F}_j$ and F_m are input to the same band-pass filter, to obtain synchronized, de-noised, dynamic top tension in the mooring lines. These are denoted $\hat{F}_{d,j}(t)$ and $F_{d,m}(t)$, respectively.

The measured dynamic tension is then compared to the one predicted by each of the N_c candidates:

$$\varepsilon_j(t) = \left(\hat{F}_{d,j}(t) - F_{d,m}(t) \right)^2 \tag{10}$$

If there is too little fairlead motion, and thus insignificant dynamic tension, no meaningful comparison can be made between the predictions and the measurement. We therefore define a threshold $F_{d,min}$, above which the error Eq. (10) is accumulated to an indicator $\Lambda_j(t)$ associated with each of the N_c candidates.

$$\Lambda_j(t) = \int_0^t K \varepsilon_j(t') \mathbf{1} \left[\min_{j \leq N_c} \hat{F}_{d,j}(t') - F_{d,min} \right] dt' \tag{11}$$

where $\mathbf{1}[\ldots]$ is the Heaviside function, equal to 1 if its argument is positive, and 0 else, and K an integrator gain. It is clear from this expression that smaller Λ_j are related to more promising candidates than larger ones. The j indices are then re-ordered to $(j_1, \ldots, j_{N_c})$, such that the most promising candidates come first: $k < k' \implies \Lambda_{j_k}(t) \leq \Lambda_{j_{k'}}(t)$.

---

5 In the present work, once the RIFLEX model of the "nominal" mooring system is set up, such parametric variations can conveniently be run automatically using the SIMA workbench [23].
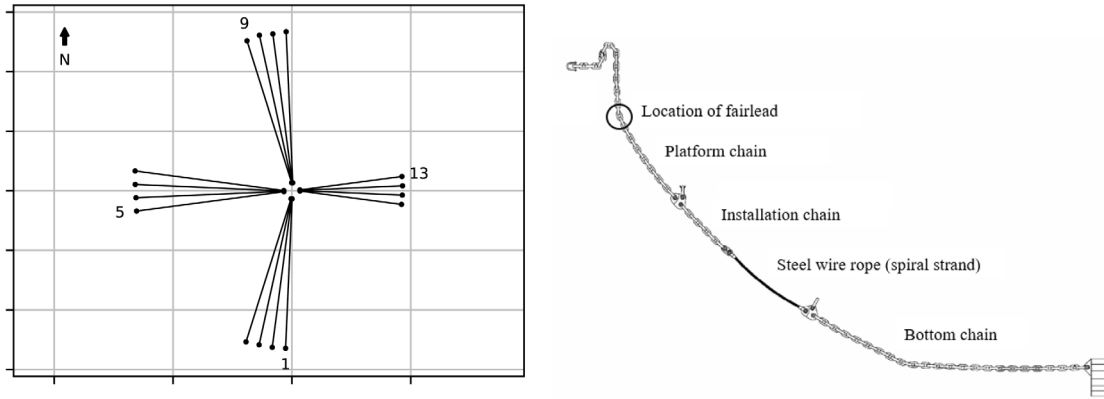
Fig. 7. Horizontal projection of mooring system (left) and mooring line composition (right, not to scale).

Once the most promising candidates are identified, the tension estimate could simply be set to $\hat{F}_{j_1}(p(t))$, which includes the (unbiased) static and dynamic tension. Doing so yields discontinuities in the tension estimate when the best candidate changes, which might not be desirable for some applications. The heuristic approach selected here is to use a weighted mean of the various $\hat{F}_{j_k}(p(t))$, with exponential weights λ_{j_k}, that strongly penalize bad candidates:

$$\lambda_{j_k}(t) = e^{\alpha\left(\frac{\Lambda_{j_1}}{\Lambda_{j_k}} - 1\right)} \tag{12}$$

The coefficient $\alpha > 0$ steers how much we want to promote the best candidate(s) compared to the following ones. The tension estimate is then

$$\hat{F}(t) = \left(\sum_{k=1}^{N_c} \lambda_{j_k}(t)\right)^{-1} \sum_{k=1}^{N_c} \lambda_{j_k}(t)\hat{F}_{j_k}(p(t)) \tag{13}$$

In the present work, $F_{\min} = 100$ kN, $\alpha = 75$ and $K = 10^6$ kN^2. The $\Lambda_j(t)$ are initialized to zero and the tension estimate Eq. (13) is output only when $\forall j \in \{1...N_c\}, \Lambda_j(t) \geq \Lambda_{\min}$, i.e. when enough relevant data (enough motions of the fairlead) has been acquired. $\Lambda_{\min}$ is set here to 0.1, Note that the present approach has similarities with dynamic hypothesis testing developed in [24] for line failure detection. This latter method is however currently limited to linear systems, which makes it inadequate for the present application, where the modelling of the mooring system's nonlinear behaviour is required.

3. Case study

The tension estimation method presented in Section 2 is now applied to a concrete case involving a semi-submersible platform installed on the Norwegian Continental Shelf.

3.1. Description of the platform and mooring

A semi-submersible FPU operating in 300 m water depth in the Norwegian Sea is considered. The platform has six columns, two pontoons with length 102.4 m at a distance of 96 m, a draught of 25 m and a total displacement of 84,848 tonnes. It is permanently moored by a spread mooring system that consists of 16 lines in clusters of four (Fig. 7). The fairleads are located approximately 68 m from the unit center, 8.8 m below the still water level. The mooring pattern is asymmetric, with shorter lines towards the east.

The mooring lines considered in the present study are lines number 1, 5, 9 and 13, as numbered in Fig. 7. Their main properties are given in Table 3. The anchor positions are based on field measurements, and the nominal lengths of the platform chains have been adjusted to obtain pretensions close to those measured on site for each of the lines. All lines are composed of a catenary chain–wire–chain configuration, with chain for the upper and lower segments, and steel wire rope in-between (Fig. 7). Mooring lines 1, 5 and 9 consist of a 120 m installation chain, a 180 m steel wire rope, and 1000 m bottom chain and four connection plates of 1.5 m each. Mooring lines 13 has a 20 m installation chain, 120 m steel wire rope, 600 m bottom chain and three connection plates of 1.5 m each.

The chain segments are made of studless R4 links, with a nominal diameter of 142 mm. Their weight in water is 3.44 kN/m, and their drag coefficient is estimated to 2.4 (wrt. nominal diameter). The steel wire rope is made of sheathed spiral strand wire, with a diameter of 156 mm (incl. 20 mm plastic sheathing). Its weight in water is 0.91 kN/m, and the drag coefficient is 1.2 (wrt. diameter including sheathing). Both segment types have a minimum breaking load larger than 16 MN.

Table 4

List of sea-states with corresponding significant wave height H_s, wave peak period T_p and mean wind velocity U_w. Sea-states 1–15 are used for the training of the ANN, while 16–30 are used for validation. Wind and wave propagation direction was 10 deg with respect to North.

Training set				Validation set			
Sea-state #	H_s [m]	T_p [s]	U_w [m/s]	Sea-state #	H_s [m]	T_p [s]	U_w [m/s]
1	1.0	14.5	4.5	16	2.0	5.5	7.0
2	1.0	20.5	4.5	17	2.0	15.5	7.0
3	2.0	1.5	7.0	18	4.0	8.5	11.4
4	4.0	10.5	11.4	19	4.0	17.5	11.4
5	5.0	5.5	13.4	20	5.0	11.5	13.4
6	6.0	17.5	15.2	21	7.0	8.5	16.9
7	7.0	13.5	16.9	22	8.0	16.5	18.5
8	8.0	8.5	18.5	23	9.0	9.5	20.0
9	11.0	15.5	22.6	24	9.0	13.5	20.0
10	12.0	12.5	23.7	25	11.0	10.5	22.6
11	12.0	14.5	23.7	26	11.0	13.5	22.6
12	12.0	16.5	23.7	27	13.0	11.5	24.7
13	13.0	14.5	24.7	28	14.0	14.5	25.7
14	13.0	15.5	24.7	29	14.0	12.5	25.7
15	15.0	17.5	26.6	30	15.0	15.5	26.6

3.2. Numerical model and motion/tension simulations

Mooring line responses are computed using time domain simulations, with a decoupled approach[6]: first, floater motions are simulated with a quasi-static representation of the mooring line forces. Then the motion from step 1 is imposed on finite-element (FE) models of the mooring lines of interest, to obtain time series of mooring line axial tension that include dynamic effects such as drag and inertia.

The first step is performed with the computer program SIMO [23], which solves the nonlinear and dynamic equation of motion in time domain with excitation from waves and wind. Waves are described by the double-peaked Torsethaugen wave spectrum [26], assuming long-crested (unidirectional) sea. Wind speed fluctuations are modelled by the NPD/ISO wind spectrum [26], with a mean wind velocity U_w related to H_s by regression made on hindcast data. The quasi-static representation of the mooring lines implies that the nonlinear restoring characteristics of the lines are accounted for, whereas dynamic effects due to drag and inertia are neglected in the SIMO analysis. The numerical model includes frequency dependent hydrodynamic coefficients for first and second order wave excitation based on potential theory, where the latter have been adjusted empirically through comparison to model test results. Frequency-dependent added mass and potential damping are represented by retardation functions. Wind loads are included by means of quadratic force coefficients. Additional damping is provided through linear and quadratic damping matrices, representing viscous damping due to columns and pontoons as well as damping contributions induced by mooring lines and risers. Quasi-static models of the risers are included to ensure that their stiffness contributions are accounted for.

The second step is performed with RIFLEX [19], using bar elements for the mooring line FE model. Geometric nonlinearities are accounted for. Drag, added mass and inertia effects on the mooring line responses are modelled. Marine growth is accounted for through increased drag coefficients and unit mass according to [27].

The sea-states used in the present case study are listed in Table 4, and have been chosen to be similar to the ones in [21, Table 1]. Wind and wave propagation direction was 10 deg, meaning that lines 1, 5, 9, 13 were solicited in very different ways: line 1 would be a "windward" line, line 9 a "leeward" line, while line 5 and 13 would experience transverse top motions. Simulations were performed for three hours in each sea-state. Candidate top segment lengths ranged from 16 m shorter than the nominal length to 24 m longer than the nominal length, by increments of 4 m. This led to $N_c = 11$ candidates. Fig. 8 shows an example of simulated fairlead motions and associated top tensions for lines 1 and 5. Note from the bottom figures that the top tension amplitude depends significantly on the line length, due to the geometric nonlinearities.

3.3. Fractal dimension of the data set

In this Section, the concepts and method described in Section 2.5, are illustrated by using the present data. The fractal dimension of four data sets are presented in Fig. 9. The first two sets are based on the *instantaneous* displacement of the fairlead $d(t)$, and the last two ones on the tadpole compression $p(t)$ of the recent history of the fairlead, with the same decay times and basis size as in Section 2. Both sets are augmented with the instantaneous tension measurement. The fractal dimension of each set is presented for each of the four lines, and as a function of the significant wave height for eight sea-states relevant for fatigue ($H_s - T_p$ pairs with a low return period).

---

[6] See e.g. [25] for a discussion on the differences between coupled and decoupled (referred to as "separated" in the reference) simulation of mooring line response.
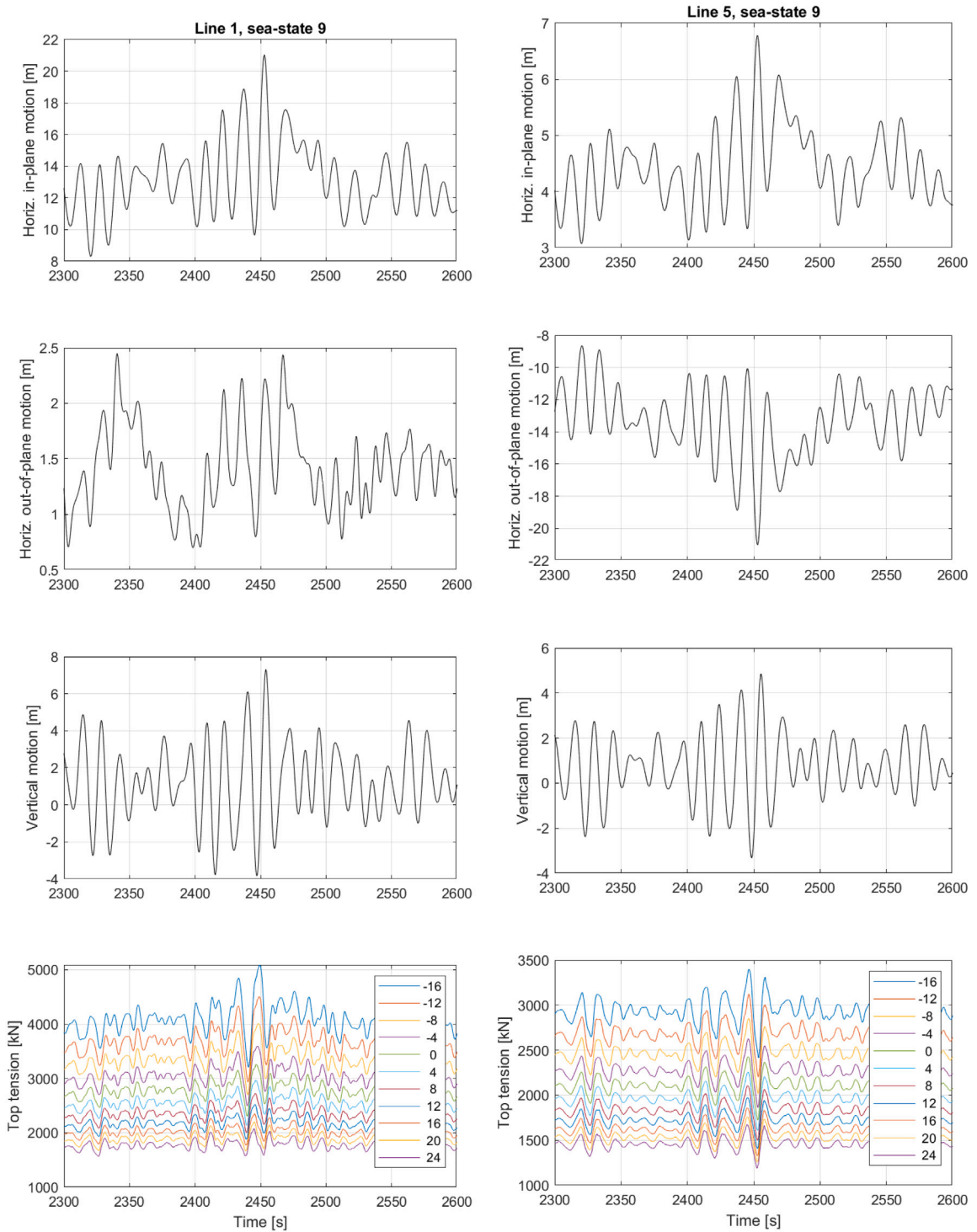
Fig. 8. Example of time series obtained from RIFLEX, and used for the training of the bank of N_c neural networks. In both plots, $H_s = 11$ m, $T_p = 15.5$ s, and $U_w = 22.6$ m/s. The data corresponding to line 1 (mostly in-line motions) and line 5 (mostly transverse motions) are shown on the left-hand side and right-hand side, respectively. The three first rows show the motions in $\{f\}$ from which p is computed. The last row shows the tensions at the fairleads for N_c line length variations compared to nominal length. The length variation in [m] is given in the legends.

The first remark is that the fractal dimensions of $\{d\}_{t \geq 0}\{d, F\}_{t \geq 0}$ are consistently different, averaging to 2.6 for the former, and to 3.2 for the latter. In other words, it will be impossible to find a functional relationship between d and F, for these sea-states
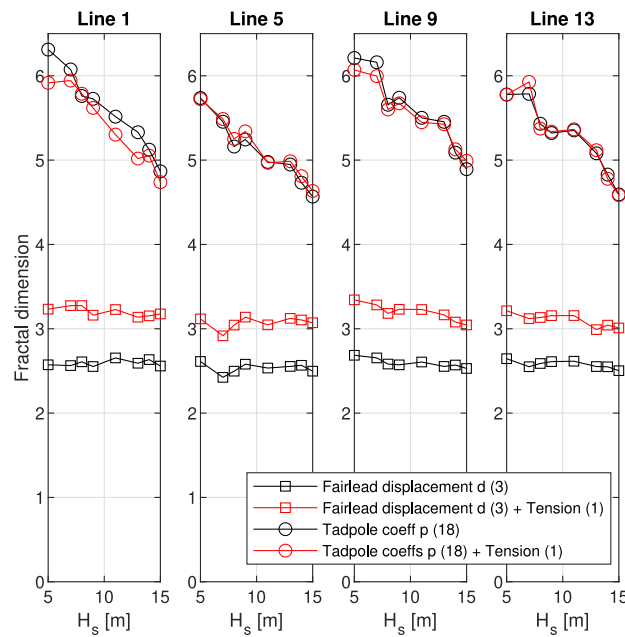
Fig. 9. Comparison of the fractal dimensions of (1) instantaneous fairlead displacements (square markers) and (2) the tadpole compression of the recent history of the fairlead displacements (circle markers). Both sets are taken alone (black), or augmented with the top tension (red). Fractal dimensions are presented as a function of H_s for sea-states of relevance for fatigue analyses, and for all four lines.

where line dynamics plays a role on the tension. On the other hand, the fractal dimensions of $\{p\}_{t\geq0}\{p,F\}_{t\geq0}$ are practically the same, indicating that there is a functional relationship, which we will do in the next section.

Interestingly, the fractal dimension of the $\{p\}_{t\geq0}$ data set decreases when increasing H_s. A physical explanation is related to the fact that for the selected sea-states, the peak wave period tends to increase with the significant wave height, and so does the typical period of the fairlead motions. These can then be described by a smaller number of elements of the basis shown in Fig. 4.

3.4. Training and validation of the ANN

The 15 first sea-states listed in Table 4 are used to generate training data for the bank of $N_c = 11$ ANN. A total of $N_{\text{training}} = 2500$ training points are selected randomly in these sea-states. For each of them, and for each of the four mooring lines, p is computed from the recent past history of the corresponding fairlead motions, and associated to the simulated tension F (for each of the N_c candidates). The training phase of the N_c neural networks takes less than one minute on a conventional laptop. Once the training was done, the corresponding sea-states were left aside, and only the 15 next ones were used for validation. Validation was performed by selecting 10^5 random instants in the validation sea-states, and comparing the tension predicted by the ANN, with the actual simulated tension. Fig. 10 shows the distribution of the tension error $\epsilon = |\hat{F} - F|$ for both the training set and the validation set. As expected the ANN performs well on the training set, with a 95th percentile of the error of less than 0.5% of the pretension in the lines. For the validation cases, not used in training, the 99th percentile of the prediction error is approximately twice as big than for the training set, which indicates good prediction and no over-fitting of the training data.

3.5. Estimator performance under normal operations

Let us now assess the performance of the estimator described in Section 2.7. To this end, synthetic "measurements" are generated by adding noise and bias to the simulated top tension, and used to assess the performance of the estimator described in Section 2.7. The noise is Gaussian, with zero mean and a standard deviation equal to 5% of the mean tension. The bias is a random number uniformly distributed between −30% and +30% of the mean tension. These synthetic "measured" tensions can be compared to the true ones by considering the grey and black curves in the top plots in Figs. 11 and 12. These figures correspond to lines 1 & 5, and 9 & 13 respectively. The actual line lengths, indicated on the third row plot, are randomly chosen, and are to be estimated. The sea-states are randomly selected among the validation set.

In each column of each figure, the first plot from the top shows the true top tension, the synthetic measurement, and the tension estimate output from the observer (which we will discuss below). The second plot shows the *dynamic* tension $\hat{F}_{d,j}$ as predicted by the N_c ANNs and as measured $\hat{F}_{d,m}$. The dynamic tensions are here obtained by an online band-pass filter with cut-off frequencies at 2 mHz and 1 Hz. The third plot shows the value of the indicator functions Λ_j defined in Eq. (11), emphasizing the indicator for the actual line length. Based on these indicators, the best and second best line lengths candidates are presented (i.e. the line
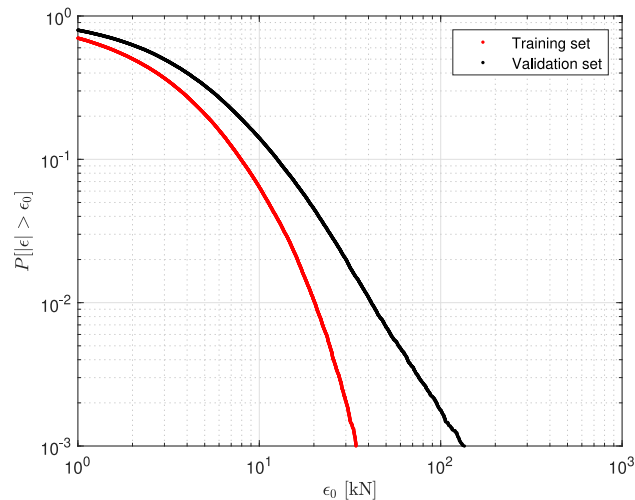
Fig. 10. Probability of exceedance of the error made by the bank of ANNs, obtained from the training set (red) and from the validation set (black). The 99th percentile of the error is 20 kN and 40 kN respectively.

lengths corresponding to candidate j_1 and j_2, according to the notation used in Section 2), on the fourth plot. The fifth plot shows the weighing factor λ_j for the two best candidates, as calculated in Eq. (12) . The weights of the following candidates are in general very small and are not represented.

The estimator is started at $t = 500$ s, after convergence of the band-pass filter, and the behaviour of the estimator is shown for the following 1000 s. For the examples involving lines 1, 5, and 9, it takes between 60 and 175 s before all indicators exceed Λ_{min} and the estimator begins to output an estimate. When this happens, the estimated tension is immediately of good quality (meaning that the length is correctly estimated at once), and does not change anymore. It is clear that strong variations in the indicator Λ_j occur when significant dynamic tension is observed, i.e. when it is possible to discriminate between the dynamic stiffness of the various candidates. For the case with line 13, the dynamic tension rarely exceeds 100 kN, and some Λ_j remain therefore smaller than Λ_{min} during the considered 500 s, meaning that no estimate is provided for this line.

3.6. Estimator performance under winching operations

We show now how the estimator behaves when winching is performed at random instants. In sea-state 28, starting from either a taut line (−16 m) or a slacker line (+20 m), 4 m of chain are paid out (i.e. the line length increases by 4 m). The estimator has been running for 500 s and the estimator provides a correct value of the tension before winching starts. The winch is activated at $t = 1000$ s, 4 m of mooring chains are payed out over 200 s. Results are shown in Fig. 13. Whether starting from a slack or taut line, the estimator converges towards the true tension after $t \simeq 1800$ s. This performance deteriorates in a calmer sea-state with less dynamic tension, where indicators would be updated at a lower pace, and it increases if a larger portion of chain was paid out due to a larger change of the dynamic tension.

3.7. Estimation robustness in presence of current

For given fairlead motions, the presence of an ambient current influences both the mean and the dynamic tension in mooring lines, due to the change in drag loads. Meanwhile, the estimator embeds no information about the influence of current on the line tension, since the bank of perceptrons is trained with simulation data obtained without current (see Section 3.2). In the present section we therefore investigate the robustness of the estimator to the presence of current: we verify whether the line length and mean tensions remain correctly estimated, in spite of an unmodelled current.

We consider a linear current profile with velocity U_c at the surface $U_c/2$ at the seabed. Note that the current velocity at the seabed would probably be less in reality, but our choice, inducing a larger parasitic loading all along the mooring line, is deliberately made for the purpose of this robustness check. The current propagates in the same direction as the waves.

Additional RIFLEX simulations are run in the same way as described in Section 3.2, including now a current with $U_c = 0.5$ m/s and $U_c = 1$ m/s, but using the same fairlead motions as for $U_c = 0$ m/s. Figs. 14 and 15 show the effect of the current velocity U_c on the mean and dynamic tension, respectively, and compare it to the effect of changing the line length by a quantity Δl. This is done for line 1 in a relevant sea-state, that contributes significantly to fatigue damage (sea-state 21, $H_s = 7$ m, $T_p = 8.5$ s, $U_w = 16.9$ m/s, see Table 4). From Fig. 14, for a realistic range of Δl and U_c values, the mean tension is found to be much more sensitive to a change of line length Δl than to U_c. This is also visible in the time series presented on the top of Fig. 15. However, the bottom plot in Fig. 15 shows that this does not hold for the dynamic (band-pass filtered) tension F_d that drives the estimation, see Eq. (10).
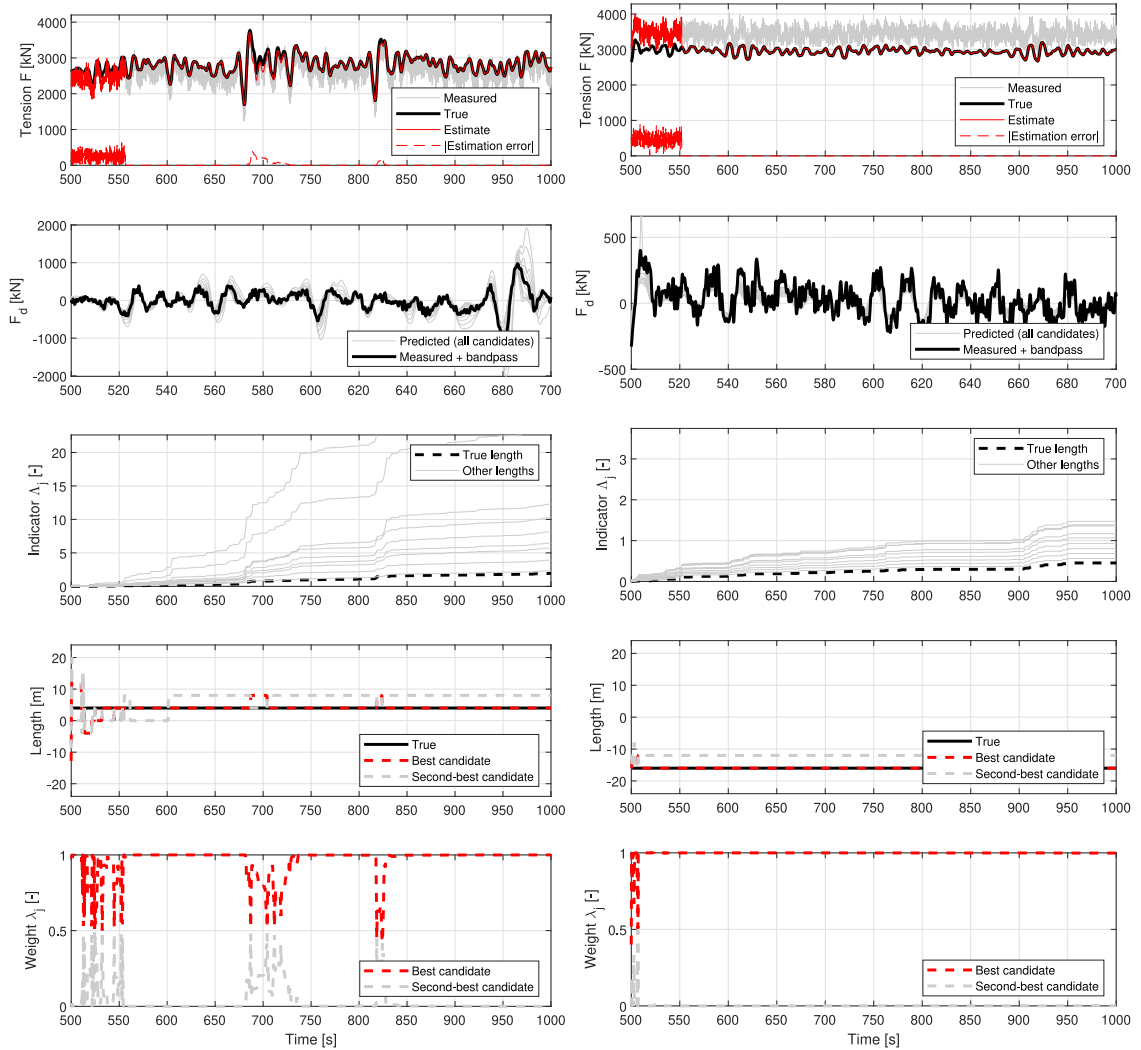
Fig. 11. Examples of performance of the estimator for line 1 (left hand side) and line 5 (r.h.s.). Sea-state and line length are chosen randomly. First row: true tension, measured tension (biased and noisy) and estimated tension as well as estimation error. Second row: true dynamic tension, and dynamic tension predicted by all ANN candidates. Third row: Λ_j-indicator accumulating the dynamic tension estimation error for all candidates. Fourth row: true line length, and length corresponding to the first and second best estimates. Fifth row: weights associated to the first and second best estimates to compute estimated tension on top plot. Note that the time-window is different for the second row, to properly represent details of the time series.

Indeed, changing the line length by $\Delta l = \pm 4$ m or increasing U_c up to 1 m/s lead to similar changes in the time-series amplitudes. The question is now whether the changes of features in the F_d time-series induced by varying U_c are sufficiently small compared to those induced by varying Δl, for the estimator to estimate Δl correctly.

This is investigated for sea-states 20–30 with $H_s \geq 5.0$ m, leading to enough line dynamics for the estimator to work correctly in nominal conditions (no current), and which have not been used in training of the perceptron. In Fig. 16, for each sea-state, the first four bars show the true change of mean tension obtained by varying Δl and U_c, the reference being the mean tension when $\Delta l = 0$ m and $U_c = 0$ m/s (nominal case). The three last bars show the variation of the estimated mean value (compared to the nominal case) output by the estimator when the spurious current velocity is 0, 0.5 or 1 m/s. The mean values are averages of the time series taken over 1000 s.

For all considered sea-states, except sea-state 20, the estimation error is similar with and without spurious current, and comparable in magnitude to the (small) change of mean tension induced by the current. For sea-state 20 and for $U_c = 1$ m/s, the estimation error is larger, and comparable to the change of mean tension induced by a change of line length. This indicates that, in this case, the estimator has failed to identify the correct line length by comparing the measured dynamic tension to the ones that have been "learned" without current. In other words, for this condition, the current affects significantly the features in F_d, compared to the ones induced by fairlead motions. This issue disappears for a lower current velocity ($U_c = 0.5$ m/s) or when the sea-state become more energetic.
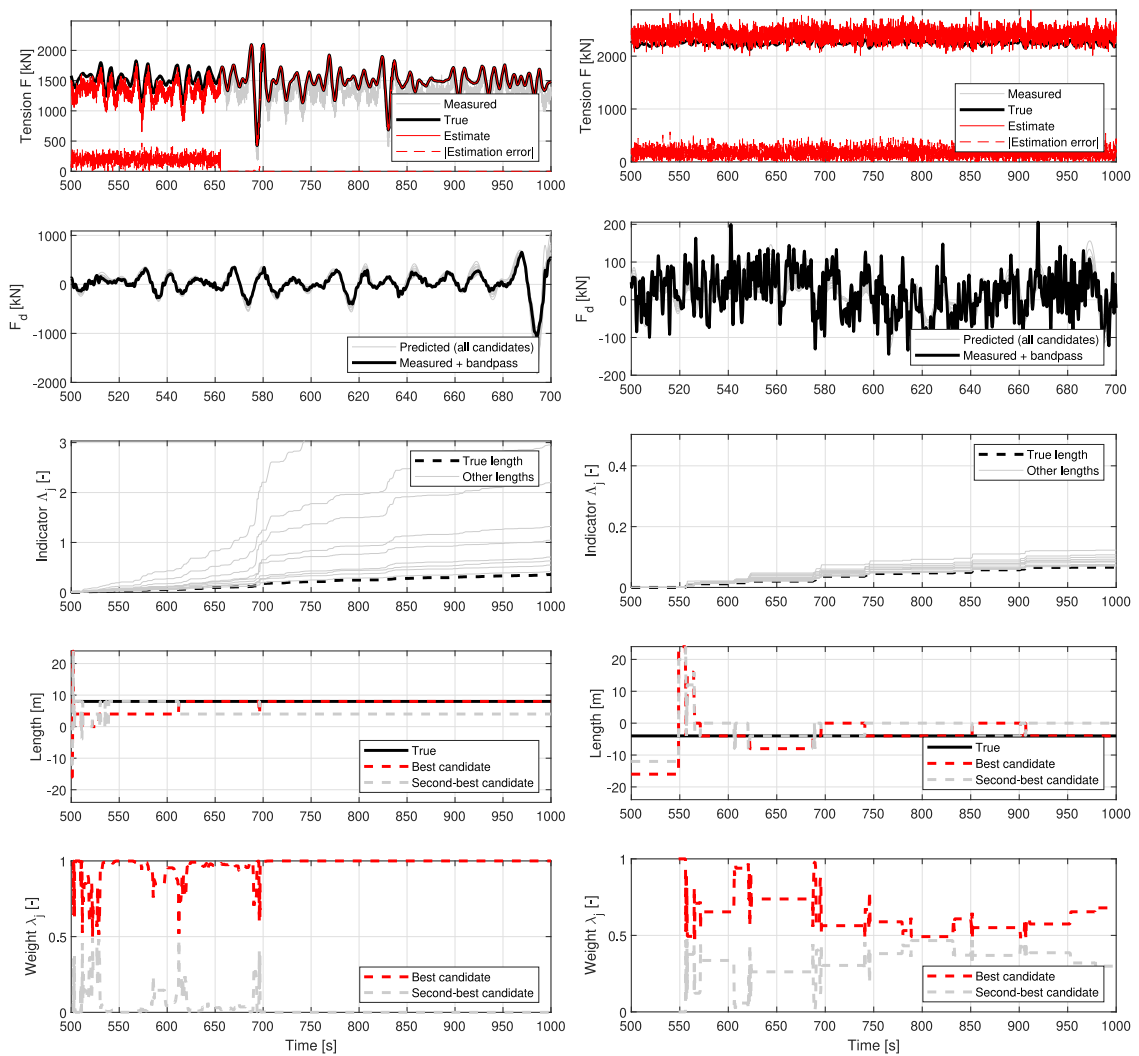
Fig. 12. Examples of performance of the estimator for line 9 (l.h.s) and 13 (r.h.s). See Fig. 11 for details.

To conclude, top tensions provided by the estimator are found to be robust to the presence of unmodelled current, if the sea-state is sufficiently energetic ($H_s > 5$ m in the present case). This corresponds to sea states that contribute to fatigue damage in North Sea climate. Robustness is achieved here because current, even with the rather conservative profile chosen in this study, has a comparatively minor effect on the dynamic tension than a change in line length. Note that if this, for another system, were not the case, an option would be to augment the estimator with perceptrons trained with simulation data including current.

4. Conclusion

Life extension of existing FPUs requires unbiased estimates of tensions in mooring lines, because the mean tension affects the fatigue damage in mooring chains. Condition-based maintenance of floating wind parks will set similar requirements because wind turbines generate a large mean thrust (especially in moderate wind conditions and sea-states), which results in large mean static loads on the mooring system.

The estimation method presented in this paper allows to correct the bias present in mooring line tension measurements. Available on-board measurements are combined with a parameterized nonlinear FEM model of the as-installed mooring system. By comparing the dynamic response of various model candidates, the unbiased estimate of the tension in the mooring is found. The presented method is based on (1) a kinematic observer, (2) the compression of the recent history of fairlead motions, (3) a bank of neural networks, each one corresponding to a given line length/static tension, and (4) a heuristic approach to selecting the most promising model among the candidates. Given that enough (wave-induced) excitation is present, the estimator converges towards the true value of the tension, and copes effectively with transients such as winching operations, and with the presence of oceanic current.
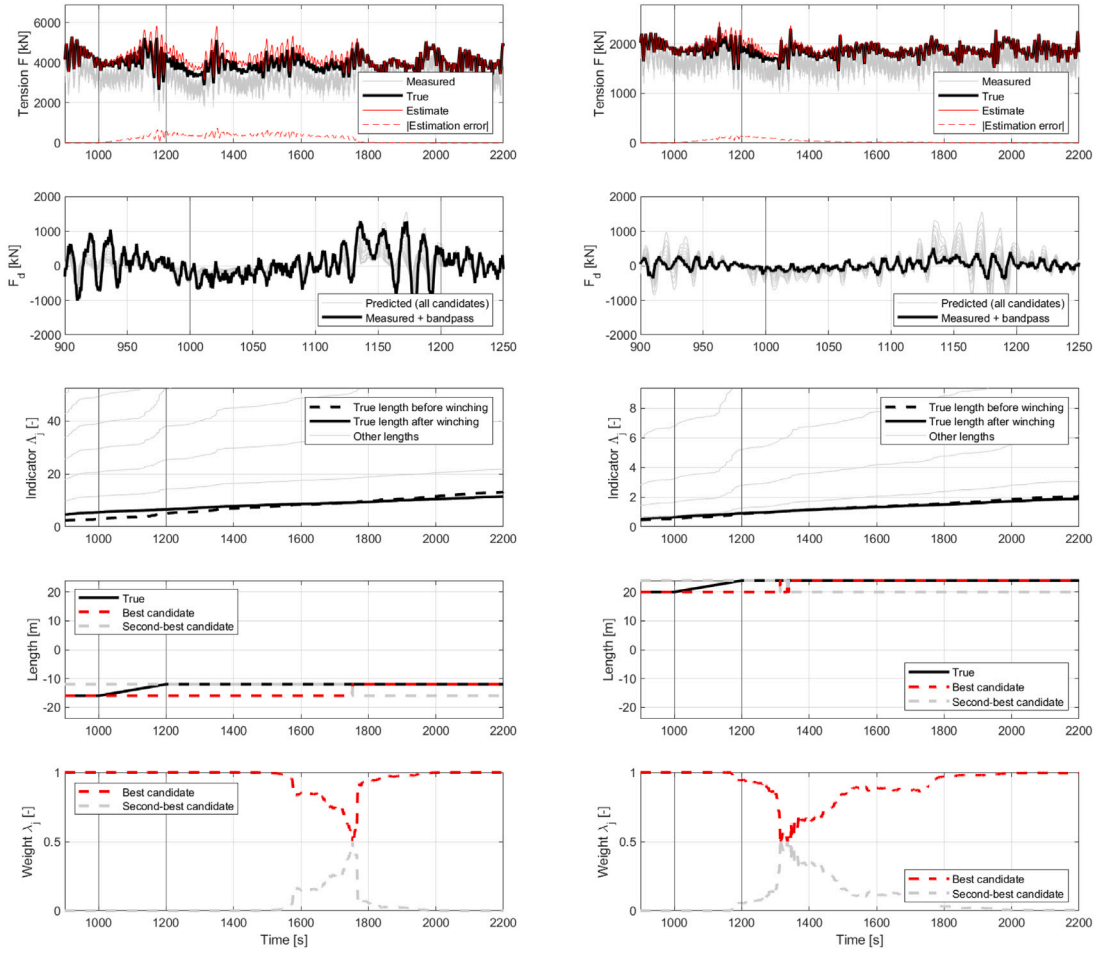
Fig. 13. Examples of winching out 4 m on line 1, starting from a taut line (l.h.s.) and slack line (r.h.s.). The winching starts at 1000 s and ends at 1200 s. See main text and Fig. 11 for details about the presented quantities. A minor difference compared to Figs. 11 and 12, is that the third row now presents the indicators corresponding to the true line lengths before and after winching.
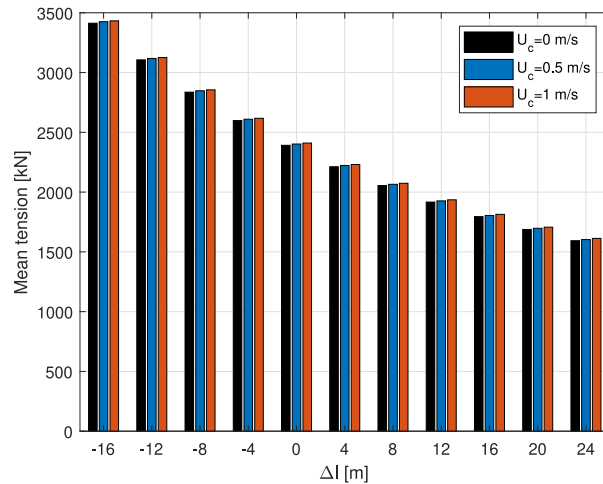

Fig. 14. Variation of the mean tension in line 1 in sea-state 21 ($H_s = 7$ m, $T_p = 8.5$ s, $U_w = 16.9$ m/s, see Table 4), in presence of current with surface velocity U_c and for various top segment lengths variations Δl.
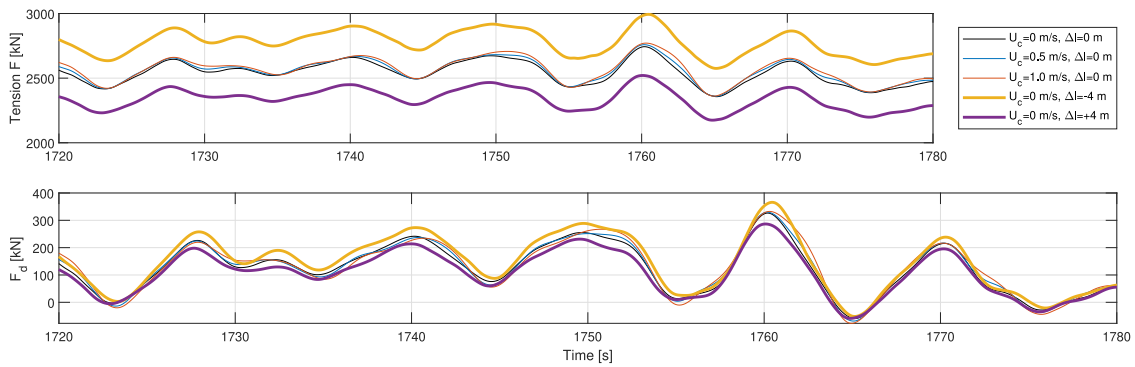
Fig. 15. Variation of the total tension F (top) and dynamic tension F_d (bottom) in line 1 in sea-state 21 ($H_s = 7$ m, $T_p = 8.5$ s, $U_w = 16.9$ m/s, see Table 4), in presence of current with surface velocity U_c and for various top segment lengths variations Δl.
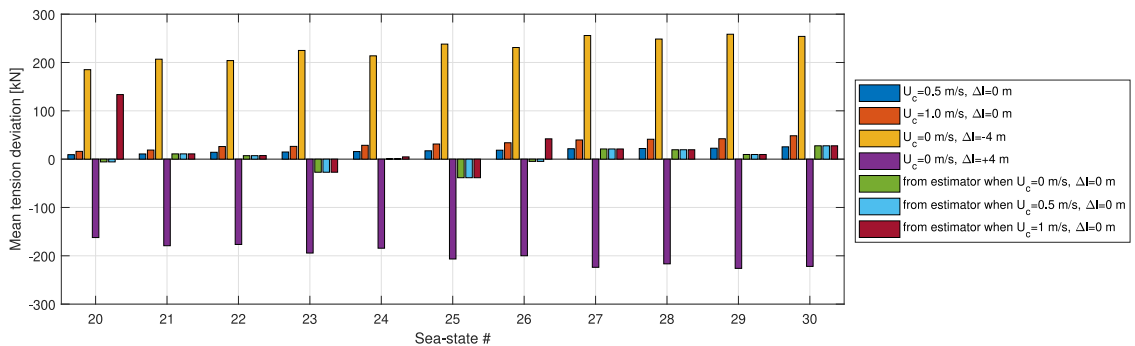

Fig. 16. Deviation of the mean tension (either true or estimated) from the nominal mean tension ($\Delta l = 0$ m, $U_c = 0$ m/s).

The computational efficiency of this method opens for on-board processing of the data (edge computing) to reduce bandwidth and storage requirements. Top tension estimates can be trivially be supplemented by other quantities of interest such as bending stresses in risers and cables at the touch-down point. This is therefore a promising generic tool for the development of complete digital twins of slender marine structures.

Ongoing work targets the validation of the estimation method for mooring systems based on field measurements. If needed, other parameters that affect the mean line tension might be added to the estimation problem. Examples are marine growth and the presence of ocean current, whose effect on top tension can be computed from nonlinear FEM. The main challenge would then lie in the large resulting number of model candidates N_c that the estimator has to choose from, and thus in a possibly poorer convergence rate.

Declaration of competing interest

The authors declare that they have no known competing financial interests or personal relationships that could have appeared to influence the work reported in this paper.

Data availability

Field data presented in Fig. 1 is confidential. Simulation data can be made available upon request.

Acknowledgements

References

[1] Kvitrud A. Anchor line failures- Norwegian Continental Shelf - 2010- 2014. Tech. rep. 992081, Petroleumtilsynet; 2014.

[2] Spong R, Garrity R, Thompson C, Yan X, Gabrielsen Ø, L'Hostis D, et al. Mooring integrity issues and lessons learned database - DeepStar® project 20401. In: Offshore technology conference, no. OTS-31823-MS. OTC; 2022, http://dx.doi.org/10.4043/31823-MS, URL https://onepetro.org/OTCONF/proceedings/22OTC/1-22OTC/D011S011R004/484370.

[3] Hørte T. Analysis of chain fatigue test data. NORMOOR JIP phase 3 report, DNV; 2020.

[4] Ma K-t, Gabrielsen Ø, Li Z, Baker D, Yao A, Vargas P, et al. Fatigue tests on corroded mooring chains retrieved from various fields in Offshore West Africa and the North Sea. In: Volume 3: structures, safety, and reliability. Glasgow, Scotland, UK: American Society of Mechanical Engineers; 2019, http://dx.doi.org/10.1115/OMAE2019-95618.

[5] Zhang Y-H, Smedley P. Fatigue performance of high strength and large diameter mooring chain in seawater. In: Volume 3: structures, safety, and reliability. Glasgow, Scotland, UK: American Society of Mechanical Engineers; 2019, http://dx.doi.org/10.1115/OMAE2019-95984.

[6] Fonseca N, Ommani B, Stansberg CT, Bøckmann A, Birknes-Berg J, Nestegård A, et al. Wave forces and low frequency drift motions in extreme seas: benchmark studies. In: Offshore technology conference. Houston, Texas, USA; 2017, http://dx.doi.org/10.4043/27803-MS.

[7] Lone EN, Larsen K, Sauder T, Leira BJ. Fatigue assessment of mooring chain considering the effects of mean load and corrosion. In: Proceedings of the ASME 2021 40th international conference on ocean, offshore and arctic engineering. 2021.

[8] Lone EN, Sauder T, Larsen K, Leira BJ. Probabilistic fatigue model for design and life extension of mooring chains, including mean load and corrosion effects. Ocean Eng 2022;245:110396. http://dx.doi.org/10.1016/j.oceaneng.2021.110396.

[9] Nærings-og fiskeridepartementet. Forskrift om posisjonerings- og ankringssystemer på flyttbare innretninger (ankringsforskriften 09). 2009.

[10] Brown M, Hall T, Marr D, English M, Snell R. Floating production mooring integrity JIP - key findings. In: Offshore technology conference. Houston, Texas; 2005, http://dx.doi.org/10.4043/17499-MS.

[11] Statoil. Ankerlinebrudd på norne, dybdestudierapport. Technical report, Statoil; 2013.

[12] Lone EN, Sauder T, Larsen K, Leira BJ. Fatigue reliability of mooring chains, including mean load and corrosion effects. Ocean Eng 2022. in Press.

[13] Kaasen KE. Study of deepsea atlantic mooring line #8 failure, TEKNA DP and mooring conference - trondheim, Norway. 2013.

[14] Aksnes V, Berthelsen PA, Da Fonseca NMMD. On the need for calibration of numerical models of large floating units against experimental data. In: The twenty-fifth international ocean and polar engineering conference. International Society of Offshore and Polar Engineers; 2015.

[15] Fossen TI. Handbook of marine craft hydrodynamics and motion control. John Wiley & Sons, Ltd; 2011.

[16] Kirkko-Jaakkola M, Collin J, Takala J. Bias prediction for MEMS gyroscopes. IEEE Sens J 2012;12(6):2157–63. http://dx.doi.org/10.1109/JSEN.2012.2185692.

[17] Mainçon P. A Wiener-laguerre model of VIV forces given recent cylinder velocities. Math Probl Eng 2011;2011:1–43. http://dx.doi.org/10.1155/2011/414702.

[18] Cybenko G. Approximation by superpositions of a sigmoidal function. Math Control Signals Systems 1989;2:303–14.

[19] SINTEF Ocean. RIFLEX 4.8.0 user manual. 2016.

[20] Guarize R, Matos N, Sagrilo L, Lima E. Neural networks in the dynamic response analysis of slender marine structures. Appl Ocean Res 2007;29(4):191–8. http://dx.doi.org/10.1016/j.apor.2008.01.002.

[21] Christiansen NH. Hybrid method simulation of slender marine structures. (Ph.D. thesis), Lyngby: DTU Mechanical Engineering : DCAMM; 2014.

[22] Zhao Y, Dong S, Jiang F, Incecik A. Mooring tension prediction based on BP neural network for semi-submersible platform. Ocean Eng 2021;223:108714. http://dx.doi.org/10.1016/j.oceaneng.2021.108714.

[23] SINTEF Ocean. SIMA 3.2 user guide. Tech. rep., 2015.

[24] Hassani V, Pascoal AM, Sørensen AJ. Detection of mooring line failures using dynamic hypothesis testing. Ocean Eng 2018;159:496–503. http://dx.doi.org/10.1016/j.oceaneng.2018.01.021.

[25] Ormberg H, Larsen K. Coupled analysis of floater motion and mooring dynamics for a turret-moored ship. Appl Ocean Res 1998;20(1–2):55–67. http://dx.doi.org/10.1016/S0141-1187(98)00012-1.

[26] DNV. Recommended practice - environmental conditions and environmental loads (DNV-RP-C205). 2014.

[27] DNV. Offshore standard - position mooring (DNV-OS-E301). 2015.